Tsinghua Science and Technology
Doi: 10.26599/TST.2026.90100017

Research Article

Joint Design of PAPR Constrained Waveform and Receiving Filter for MIMO-OTFS ISAC System

Jiawei Feng, Jinfeng Hu, Kai Zhong (✉), Xiangqing Xiao, Jiacheng Gou, Kaizhi Ruan, Yiran Zhang and Jun Liu

Abstract Waveform design is a critical technology for orthogonal time-frequency space (OTFS) integrated sensing and communication (ISAC) systems. Existing research mainly focuses on the design of multiple-input multiple-output (MIMO)-OTFS communication waveforms or the design of dual-functional OTFS waveforms for single-input single-output (SISO) systems, which results in degraded performance in dynamic, multi-user ISAC scenarios. To address these limitations, the paper mainly investigates waveform optimization for MIMO-OTFS ISAC systems, which formulates the problem as minimizing the weighted integrated sidelobe level (WISL) under peak-to-average power ratio (PAPR) and multi-user interference (MUI) energy constraints. Due to its non-convex nature with multiple constraints, the problem is challenging to solve. To address the complicated optimization problem, an adaptive penalty analytic subproblem decomposition (APASD) method is proposed. First, auxiliary variables are introduced to decompose the original problem into several subproblems with analytic solutions. Then, leveraging the structure of the subproblems, we derive the corresponding analytic solutions. Finally, the penalty parameters are adaptively updated based on the residuals, and the overall problem is iteratively refined until convergence. Simulation results demonstrate that the proposed method can achieve a lower sidelobe level while ensuring the achievable sum-rate, and shows better performance than existing methods.

Keywords MIMO-OTFS, ISAC, waveform design, WISL, PAPR, adaptive penalty analytic subproblem decomposition (APASD)

1 Introduction

Waveform design plays a pivotal role in orthogonal time-frequency space (OTFS) integrated sensing and communication (ISAC) systems. Emerging applications such as vehicle to everything (V2X) and unmanned aerial vehicle (UAV) [1–3] impose stringent requirements on both high-speed data transmission and accurate environmental sensing, thereby accelerating the development of ISAC technologies [4–8]. With the growing demands for high-reliability communications and precise sensing, OTFS has gained prominence due to its robustness in high-speed time-varying channels and effective utilization of delay-Doppler (DD) diversity [9–12]. These advantages have consequently motivated significant research efforts on OTFS-ISAC waveform design [13–17].

The existing OTFS waveform design methods can generally be divided into two categories: 1) the multiple-input multiple-output (MIMO)-OTFS communication waveform design which neglects the requirements of the system for complex environmental sensing [18–21]; 2) dual-functional OTFS waveform design for single-input single-output (SISO) systems which reduces multi-user communication and sensing capability due to limited channels [22–25].

For the first category, [20] proposed a MIMO-OTFS downlink waveform design capable of achieving effective communication performance through precoding and intelligent

• Jiawei Feng, Jinfeng Hu, Kai Zhong and Xiangqing Xiao are with the School of Information and Communication Engineering, University of Electronic Science and Technology of China (UESTC), Chengdu 611731, China, and also with the Yangtze Delta Region Institute (Quzhou), UESTC, Quzhou 324000, China. E-mail: 202352012006@std.uestc.edu.cn; hujf@uestc.edu.cn; kzhong@uestc.edu.cn; 202211012218@std.uestc.edu.cn.
• Jiacheng Gou is with the School of Information and Communication Engineering, UESTC, Chengdu 611731, China. E-mail: jcgou@std.uestc.edu.cn.
• Kaizhi Ruan is with the National Key Laboratory of Automatic Target Recognition, Shanghai Electro-mechanical Engineering Institute, Shanghai 201109, China. E-mail: ruankaizhi@126.com.
• Yiran Zhang is with the National Key Laboratory of Digital and Agile Aircraft Design, AVIC Chengdu Aircraft Design and Research Institute, 610073 Chengdu, China. E-mail: zyrsim@163.com.
• Jun Liu is with The 41st Institute of CETC, Qingdao 266555, China. E-mail: 13863967520@139.com.
Manuscript received: 2025-09-17; revised: 2025-11-28; accepted: 2026-01-28

reflecting surfaces (IRS), while resulting in high computational complexity. [21] proposed an IRS-assisted single-user MIMO-OTFS detection method with maximum ratio combining (MRC), which lowers computational complexity, though its overall performance is still limited. However, both of the above methods do not consider the sensing requirements of MIMO-OTFS systems in multi-user scenarios.

For the second category, [24] developed a dual-functional OTFS waveform capable of suppressing radar local sidelobes. However, its performance is constrained by the constant modulus (CM) requirement, preventing ideal communication performance. [25] proposed a single-antenna low peak-to-average power ratio (PAPR) waveform design, separating the sensing and communication parts via pilot and data matrices, respectively, which improves communication quality. However, due to the limitations of the SISO system, multi-user communication and sensing performance remain constrained.

To address these issues and enhance weak targets detection without compromising MIMO-OTFS communication quality, we model the waveform design as a weighted integrated sidelobe level (WISL) minimization problem subject to multi-user interference (MUI) energy constraint. Considering the properties of OTFS modulation, PAPR constraint is included on the transmitted waveform. Furthermore, mismatched filtering is introduced to increase the degrees of freedom (DoF) in local sidelobe suppression, allowing for satisfactory communication and sensing performance at low PAPR under a preset signal-to-noise ratio (SNR) loss.

Owing to the presence of multiple constraints, the above optimization problem remains difficult to solve. We observe that the constraints in this problem can be decomposed into tractable convex quadratic forms. Based on this insight, an adaptive penalty analytic subproblem decomposition (APASD) method is proposed. Firstly, auxiliary variables are introduced to partition the original optimization problem into multiple subproblems with analytic solutions. Subsequently, the structure of these subproblems is exploited to derive the closed-form expressions. Finally, residual-based adaptive updates of the penalty parameter are performed, and the overall optimization problem is iteratively refined until convergence, thereby ensuring both efficiency and accuracy.

The main contributions of this paper mainly include:

(1) **MIMO-OTFS ISAC waveform design**: Different from existing methods, which primarily design MIMO-OTFS communication waveforms or SISO-OTFS dual-functional waveforms, this paper proposes a novel MIMO-OTFS ISAC waveform optimization model. The model demonstrates strong applicability in multi-user high-speed scenarios.

(2) **Analytic subproblem decomposition framework**: The formulated waveform design problem involves non-convex objective function and non-smooth inequality constraints, resulting in a highly coupled and non-convex optimization that is hard to solve by existing methods. To address these challenges, we propose an optimization framework that introduces auxiliary variables to partition the original problem into analytically solvable subproblems, derives analytic solutions by exploiting their structure, and adaptively updates penalty parameter until convergence.

(3) **Superior performance**: Simulation results show that the proposed method significantly improves sensing performance under specific MUI energy constraint, achieving 30 dB deeper nulls for WISL compared to ADMM [26] and 10 dB deeper nulls compared to Method [25].

Notations: The notations used in this article are listed in Table 1.

Table 1 List of Notations.

Symbol	Definition
$\mathbf{A}$	Matrix
$\mathbf{a}$	Vector
$\mathbf{I}$	Identity matrix
$(\cdot)^{*}$, $(\cdot)^{\top}$, $(\cdot)^{\mathrm{H}}$	Conjugate, transpose and conjugate transpose
$\lvert\cdot\rvert$, $\lVert\cdot\rVert$, $\lVert\cdot\rVert_F$	Magnitude, Euclidian norm, and Frobenius norm
$\otimes$, $\odot$	Kronecker product and Hadamard product
$vec\left(\cdot\right)$	Vectorization operator
$diag\left[\cdot\right]$	Diagonal operator
$\mathbb{R}$, $\mathbb{C}$	Domain of real and complex numbers
$\mathbb{E}\left(\cdot\right)$	Expectation of a random variable

2 System Model and Problem Formulation

In this section, we consider a MIMO-OTFS ISAC system consisting of K antennas and U single-antenna high-speed users, as shown in Fig. 1. The communication and sensing aspects of the system are modeled as an optimization problem, which incorporates multiple practical constraints, including the PAPR, MUI energy and SNR loss constraints.

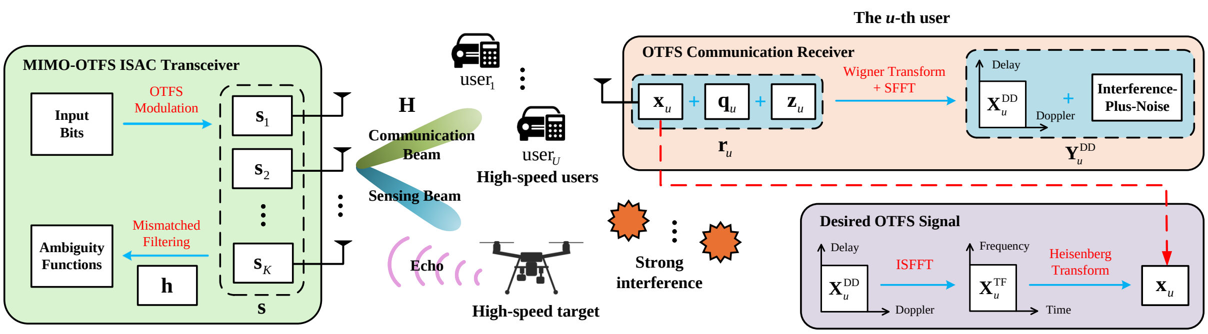

Fig. 1 MIMO-OTFS ISAC system model.

2.1 MIMO-OTFS Signal Model

Consider a time-domain signal $x_u(t)$ of an OTFS frame for the u-th single user with M subcarriers and N time slots, where the duration of each time slot is T and the subcarrier spacing is $1/T$. The information symbol matrix $\mathbf{X}_u^{\mathrm{DD}} \in \mathbb{C}^{M\times N}$ for the u-th single user is modulated by the constellation $\mathcal{A}$ in the DD domain. By performing the inverse symplectic finite Fourier transform (ISFFT) [27, 28] on $\mathbf{X}_u^{\mathrm{DD}}$, the time-frequency domain symbol matrix $\mathbf{X}_u^{\mathrm{TF}}$ can be obtained, denoted as

$$\mathbf{X}_u^{\mathrm{TF}} = \mathbf{F}_M \mathbf{X}_u^{\mathrm{DD}} \mathbf{F}_N^{\mathrm{H}}, \tag{1}$$

where $\mathbf{F}_N \in \mathbb{C}^{N\times N}$ is the Fourier transform matrix which satisfies $\mathbf{F}_N^{\mathrm{H}}\mathbf{F}_N = \mathbf{I}_N$.

By performing the Heisenberg transform [24, 29] which using a M-point inverse fast Fourier transform (IFFT) along with the pulse shaping waveform $g_{\mathrm{tx}}(t)$, the time-domain signal $x_u(t)$ can be derived. After sampling $x_u(t)$ at the frequency of M/T, we can get the discrete-time representation of OTFS signal for the u-th single downlink user

$$\mathbf{X}_u = \mathbf{G}_{tx}\mathbf{F}_M^{\mathrm{H}}\left(\mathbf{F}_M \mathbf{X}_u^{\mathrm{DD}} \mathbf{F}_N^{\mathrm{H}}\right) = \mathbf{G}_{tx}\mathbf{X}_u^{\mathrm{DD}}\mathbf{F}_N^{\mathrm{H}}, \tag{2}$$

where $\mathbf{G}_{tx} \in \mathbb{C}^{M\times M}$ is the diagonal matrix of $g_{\mathrm{tx}}(t)$ with M/T as the sampling frequency and we consider the rectangular pulse, which makes $\mathbf{G}_{tx} = \mathbf{I}_M$. The matrix $\mathbf{X}_u \in \mathbb{C}^{M\times N}$ is vectorized to get $MN \times 1$ vector

$$\mathbf{x}_u = \mathrm{vec}\left(\mathbf{X}_u\right) = \left(\mathbf{F}_N^{\mathrm{H}} \otimes \mathbf{I}_M\right)\mathbf{x}_u^{\mathrm{DD}}, \tag{3}$$

where $\mathbf{x}_u^{\mathrm{DD}} = \mathrm{vec}\left(\mathbf{X}_u^{\mathrm{DD}}\right) \in \mathbb{C}^{L\times 1}$, $L = MN$. For the MIMO-OTFS system, the OTFS signal for U downlink users is $\mathbf{x} = \left[\mathbf{x}_1^\top, \mathbf{x}_2^\top, \ldots, \mathbf{x}_U^\top\right]^\top \in \mathbb{C}^{LU\times 1}$.

2.2 MIMO-OTFS Communication Model

In the MIMO-OTFS system, each antenna independently transmits the OTFS signal through a time-varying multipath wireless channel to a single user [30]. The signal $r^{u,k}(t)$ received by the u-th user from the k-th transmit antenna is represented as

$$\begin{aligned} r^{u,k}(t) = &\iint h^{u,k}(\tau,\nu)s_k(t-\tau)e^{j2\pi\nu(t-\tau)}d\tau d\nu \\ &+ w^{u,k}(t), \end{aligned} \tag{4}$$

where $s_k(t)$ is the transmitted waveform of the k-th antenna and the transmitted waveform of the whole system can be written as vector form $\mathbf{s} = \left[\mathbf{s}_1^\top, \mathbf{s}_2^\top, \ldots, \mathbf{s}_K^\top\right]^\top \in \mathbb{C}^{LK\times 1}$. Due to the sparsity of the channel, $h^{u,k}(\tau,\nu)$ can be expressed as

$$h^{u,k}(\tau,\nu) = \sum_{i=1}^{P^{u,k}} h_i^{u,k}\delta(\tau - \tau_i^{u,k})\delta(\nu - \nu_i^{u,k}), \tag{5}$$

where $\delta(\cdot)$ is Dirac delta function, $P^{u,k}$ is the number of propagation paths. $h_i^{u,k}$, $\tau_i^{u,k}$ and $\nu_i^{u,k}$ denote the complex path gain, delay, and Doppler shift of the i-th path [31]. We write (5) in matrix form

$$\mathbf{H}^{u,k} = \sum_{i=1}^{P^{u,k}} h_i^{u,k}\mathbf{\Psi}_{a_i^{u,k}}\mathbf{\Xi}_{b_i^{u,k}}, \tag{6}$$

where

$$\mathbf{\Psi}_{a_i^{u,k}} = \begin{bmatrix} \mathbf{0}_{(L-a_i^{u,k})\times a_i^{u,k}} & \mathbf{I}_{L-a_i^{u,k}} \\ \mathbf{I}_{a_i^{u,k}} & \mathbf{0}_{a_i^{u,k}\times(L-a_i^{u,k})} \end{bmatrix}, \tag{7}$$

$$\mathbf{\Xi}_{b_i^{u,k}} = \mathrm{diag}\left[1, e^{-\frac{j2\pi b_i^{u,k}}{L}}, \cdots, e^{-\frac{j2\pi(L-1)b_i^{u,k}}{L}}\right]. \tag{8}$$

When considering the entire MIMO-OTFS system, the effective channel matrix is given by

$$\mathbf{H} = \begin{bmatrix} \mathbf{H}^{1,1} & \mathbf{H}^{1,2} & \cdots & \mathbf{H}^{1,K} \\ \mathbf{H}^{2,1} & \mathbf{H}^{2,2} & \cdots & \mathbf{H}^{2,K} \\ \vdots & \vdots & \ddots & \vdots \\ \mathbf{H}^{U,1} & \mathbf{H}^{U,2} & \cdots & \mathbf{H}^{U,K} \end{bmatrix}, \tag{9}$$

and we can get the discrete form of the received signal

$$\mathbf{r} = \mathbf{H}\mathbf{s} + \mathbf{z}, \tag{10}$$

where $\mathbf{z} = \left[\mathbf{z}_1^\top, \mathbf{z}_2^\top, \ldots, \mathbf{z}_U^\top\right]^\top \in \mathbb{C}^{LU\times 1}$ is the noise vector, with $\mathbf{z}_u \sim \mathcal{CN}(0, N_0\mathbf{I}_L)$, N_0 is the noise power. To get the desired OTFS signal $\mathbf{x}$ for the downlink users, (10) can be rewritten as

$$\mathbf{r} = \mathbf{x} + \underbrace{(\mathbf{H}\mathbf{s} - \mathbf{x})}_{\text{MUI}} + \mathbf{z}, \tag{11}$$

where $\mathbf{r} = \left[\mathbf{r}_1^\top, \mathbf{r}_2^\top, \ldots, \mathbf{r}_U^\top\right]^\top \in \mathbb{C}^{LU\times 1}$.

By performing the Wigner transform and symplectic finite Fourier transform (SFFT) [32, 33], we can get the vector form of the DD domain symbols at the u-th receiver

$$\mathbf{y}_u^{\mathrm{DD}} = (\mathbf{F}_N \otimes \mathbf{G}_{rx})\,\mathbf{r}_u, \tag{12}$$

where $\mathbf{y}^{\mathrm{DD}} = \mathrm{vec}\left(\mathbf{Y}_u^{\mathrm{DD}}\right)$, $\mathbf{Y}_u^{\mathrm{DD}}$ is the DD domain symbol matrix. $\mathbf{G}_{rx} \in \mathbb{C}^{M\times M}$ is the receiving pulse shaping filter. In this work, a rectangular pulse is assumed, which makes $\mathbf{G}_{rx} = \mathbf{I}_M$. Let $\mathbf{q}_u = \sum_{k=1}^{K} \mathbf{H}^{u,k}\mathbf{s}_u - \mathbf{x}_u$, $\mathbf{H}\mathbf{s} - \mathbf{x} = \left[\mathbf{q}_1^\top, \mathbf{q}_2^\top, \ldots, \mathbf{q}_U^\top\right]^\top \in \mathbb{C}^{LU\times 1}$ and (12) can be rewritten as

$$\begin{aligned}
\mathbf{y}_u^{\mathrm{DD}} &= (\mathbf{F}_N \otimes \mathbf{I}_M)\,\mathbf{x}_u + (\mathbf{F}_N \otimes \mathbf{I}_M)\,\mathbf{q}_u \\
&\quad + (\mathbf{F}_N \otimes \mathbf{I}_M)\,\mathbf{z}_u \\
&= (\mathbf{F}_N \otimes \mathbf{I}_M)\left(\mathbf{F}_N^{\mathrm{H}} \otimes \mathbf{I}_M\right)\mathbf{x}_u^{\mathrm{DD}} \\
&\quad + \mathbf{q}_u^{\mathrm{DD}} + \mathbf{z}_u^{\mathrm{DD}} \\
&= \mathbf{x}_u^{\mathrm{DD}} + \mathbf{q}_u^{\mathrm{DD}} + \mathbf{z}_u^{\mathrm{DD}},
\end{aligned} \tag{13}$$

where $\mathbf{q}_u^{\mathrm{DD}} = (\mathbf{F}_N \otimes \mathbf{I}_M)\,\mathbf{q}_u$ and $\mathbf{z}_u^{\mathrm{DD}} = (\mathbf{F}_N \otimes \mathbf{I}_M)\,\mathbf{z}_u$. To evaluate the performance of the communication system, the achievable sum-rate is typically employed. For the u-th user, the signal-to-interference-plus-noise ratio (SINR) per OTFS frame is given as

$$\omega_u = \frac{\|\mathbf{x}_u^{\mathrm{DD}}\|^2}{\|\mathbf{q}_u^{\mathrm{DD}}\|^2 + \|\mathbf{z}_u^{\mathrm{DD}}\|^2}, \tag{14}$$

The matrix $\mathbf{F}_N \otimes \mathbf{I}_M$ is unitary, i.e., it satisfies $(\mathbf{F}_N \otimes \mathbf{I}_M)^{\mathrm{H}}(\mathbf{F}_N \otimes \mathbf{I}_M) = \mathbf{I}_{MN}$, which makes

$$\begin{aligned}
\|\mathbf{x}_u^{\mathrm{DD}}\|^2 &= \mathbf{x}_u^{\mathrm{H}}(\mathbf{F}_N \otimes \mathbf{I}_M)^{\mathrm{H}}(\mathbf{F}_N \otimes \mathbf{I}_M)\,\mathbf{x}_u \\
&= \|\mathbf{x}_u\|^2.
\end{aligned} \tag{15}$$

Similarly, we have $\|\mathbf{q}_u^{\mathrm{DD}}\|^2 = \|\mathbf{q}_u\|^2$ and $\|\mathbf{z}_u^{\mathrm{DD}}\|^2 = \|\mathbf{z}_u\|^2 = N_0 L$. Accordingly, the achievable sum-rate can be written as

$$\begin{aligned}
\mathrm{ASR} &= \sum_{u=1}^{U} \log_2(1 + \omega_u) \\
&= \sum_{u=1}^{U} \log_2\Big(1 + \frac{\|\mathbf{x}_u\|^2}{\|\mathbf{q}_u\|^2 + N_0 L}\Big).
\end{aligned} \tag{16}$$

Since $\mathbf{x}_u$ was modulated by the constellation $\mathcal{A}$ with fixed energy, $\|\mathbf{x}_u\|^2$ is also fixed. Hence, the achievable sum-rate can be maximized by minimizing the MUI energy, which is denoted as

$$\mathrm{P}_{\mathrm{MUI}}(\mathbf{s}) = \|\mathbf{H}\mathbf{s} - \mathbf{x}\|^2. \tag{17}$$

2.3 MIMO-OTFS Sensing Model

Due to the non-constant envelope of OTFS signal in the time domain, it is highly challenging to design waveforms that can simultaneously ensure low PAPR, low sidelobe level and reliable communication performance [34–36]. To overcome this difficulty, we consider the joint design of the transmitted waveform and the receiving filter.

For the transmitted signal vector $\mathbf{s}$ and receiving filter $\mathbf{h} = \left[\mathbf{h}_1^\top, \mathbf{h}_2^\top, \ldots, \mathbf{h}_K^\top\right]^\top \in \mathbb{C}^{LK\times 1}$, the ambiguity function (AF) between them is denoted as

$$\mathrm{AF}_{k_1,k_2}(d, f) = \mathbf{h}_{k_2}^{\mathrm{H}}\mathbf{J}_d\mathbf{D}_f\mathbf{s}_{k_1}, k_1, k_2 = 1, 2, \ldots, K, \tag{18}$$

where

$$\mathbf{J}_d = \begin{bmatrix} \mathbf{0}_{(L-d)\times d} & \mathbf{I}_{L-d} \\ \mathbf{0}_d & \mathbf{0}_{d\times(L-d)} \end{bmatrix}, \mathbf{J}_{-d} = \mathbf{J}_d^\top, \tag{19}$$

$$\mathbf{D}_f = \mathrm{diag}\left[1, e^{-\frac{j2\pi f}{L}}, \cdots, e^{-\frac{j2\pi(L-1)f}{L}}\right]. \tag{20}$$

To enhance the target detection capability within specific delay-Doppler regions, we constrain integrated sidelobe level (ISL) minimization to a local region of interest rather than the full domain. Denote the interested area of auto-ambiguity function (AAF) $\mathbf{\Omega}_a = \{(d, f) \mid d \in \mathbf{\Omega}_a^D, f \in \mathbf{\Omega}_a^F\}$ and cross-ambiguity function (CAF) $\mathbf{\Omega}_c = \{(d, f) \mid d \in \mathbf{\Omega}_c^D, f \in \mathbf{\Omega}_c^F\}$, where $\mathbf{\Omega}_a^D$, $\mathbf{\Omega}_c^D$ denote the delay indices, and $\mathbf{\Omega}_a^F$, $\mathbf{\Omega}_c^F$ denote the Doppler indices. Accordingly, the WISL metric is defined as (21), where $w_a(d, f)$ and $w_c(d, f)$ are the weight matrices [25] of AAF and CAF, respectively, which can be expressed as

$$w_a(d, f) = \begin{cases} 1, & (d, f) \in \mathbf{\Omega}_a \\ 0, & \text{otherwise} \end{cases}, \tag{22}$$

$$w_c(d, f) = \begin{cases} 1, & (d, f) \in \mathbf{\Omega}_c \\ 0, & \text{otherwise} \end{cases}. \tag{23}$$

The mainlobe level should not be suppressed so that $w_a(0, 0) = 0$.

The joint design of the waveform and receiving filter enhances design flexibility by introducing additional degrees of freedom (DoF), but this inevitably incurs SNR loss at the receiver [37–39]. The SNR loss associated with the mismatched filter in a multi-channel system, as compared to the matched filter baseline, is given by

$$\mathrm{SNRL} = \max_{k=1,2,\ldots,K} \mathrm{SNRL}_k, \tag{24}$$

where

$$\mathrm{SNRL}_k = 10\log_{10}\frac{\|\mathbf{h}_k\|^2\|\mathbf{s}_k\|^2}{|\mathbf{h}_k^{\mathrm{H}}\mathbf{s}_k|^2}. \tag{25}$$

$$\mathrm{WISL}(\mathbf{s},\mathbf{h}) = \sum_{(d,f)\in\mathbf{\Omega}_a}\sum_{k_1=1}^{K}\sum_{\substack{k_2=1\\k_2=k_1}}^{K} w_a(d,f)\left|\mathrm{AF}_{k_1,k_2}(d,f)\right|^2 + \sum_{(d,f)\in\mathbf{\Omega}_c}\sum_{k_1=1}^{K}\sum_{\substack{k_2=1\\k_2\neq k_1}}^{K} w_c(d,f)\left|\mathrm{AF}_{k_1,k_2}(d,f)\right|^2 \quad (21)$$

Assume the energy of k-th transmitted waveform is constrained by $\|\mathbf{s}_k\|^2 = \mathcal{E}$ and the energy of k-th receiving filter is constrained by $\|\mathbf{h}_k\|^2 = \mathcal{H}$, the SNR loss can be controlled by incorporating the following constraint function

$$\mathrm{PL}(\mathbf{s}_k,\mathbf{h}_k) = \left|\mathbf{h}_k^{\mathrm{H}}\mathbf{s}_k - P_m\right|^2, \quad (26)$$

where P_m is the predefined peak value. The relationship between P_m and the predefined SNR loss η (in dB) is $P_m = \sqrt{\mathcal{E}\mathcal{H}}/10^{-\eta/20}$. Thus, we can control the SNR loss through the above constraint function [40].

2.4 Problem Formulation

Since the OTFS signal is non-constant modulus in the time domain, to control its amplitude and prevent nonlinear distortion during transmission, it is necessary to consider the PAPR constraint. Given that the transmitted waveform energy is constant for each antenna, the PAPR [25, 41] is evaluated separately for each antenna

$$\mathrm{PAPR}(\mathbf{s}_k) = \frac{1}{\mathbb{E}\left(|\mathbf{s}_k(l)|^2\right)}\max_{l=1,2,\ldots,L}|\mathbf{s}_k(l)|^2. \quad (27)$$

To enhance the detection capability of weak targets while ensuring communication performance, it is necessary to minimize WISL while controlling the MUI energy and SNR loss. In addition, to prevent nonlinear distortion caused by high PAPR of the OTFS system, the energy and PAPR of the waveform transmitted by each antenna need to be constrained. In summary, the corresponding optimization problem can be formulated as

$$\begin{aligned} \min_{\mathbf{s},\mathbf{h}}\ & \mathrm{WISL}(\mathbf{s},\mathbf{h}) \\ \text{s.t. } & \|\mathbf{s}_k\|^2 = \mathcal{E}, \\ & \|\mathbf{h}_k\|^2 = \mathcal{H}, \\ & \mathrm{PAPR}(\mathbf{s}_k) \leqslant \rho, \\ & \mathrm{PL}(\mathbf{s}_k,\mathbf{h}_k) \leqslant \theta, \\ & \mathrm{P_{MUI}}(\mathbf{s}) \leqslant \epsilon, \end{aligned} \quad (28)$$

where $k = 1,2,\ldots,K$, $\mathcal{E}$ is the energy of the waveform transmitted by each antenna, $\mathcal{H}$ is the energy of corresponding receiving filter, $\rho \geqslant 1$ is the PAPR threshold, $\theta \geqslant 0$ is the peak matching threshold and $\epsilon \geqslant 0$ is the MUI energy threshold.

The non-convex nature of the original problem arises from the bilinear coupling between waveform and filter variables, under separate energy constraints. In addition, the inclusion of multiple inequality constraints further exacerbates the problem's computational intractability. To overcome this, we propose a structural subproblem reconstruction strategy in the next subsection. This strategy systematically decomposes the original problem into a set of analytically solvable subproblems. By integrating the optimal solutions of these subproblems, the method can achieve better solutions, or even a globally optimal solution.

3 The Proposed APASD Framework

For the multiple inequality constraints contained in (28), existing methods mainly solve them through the ADMM framework. However, due to the coupling of complex constraints, the decomposed subproblems can only obtain approximate solutions, resulting in performance degradation and slow convergence. We observe that, by reformulating the problem, the constraints in this problem can be decomposed into tractable convex quadratic forms. By introducing auxiliary variables, the original problem can be decomposed into multiple simple subproblems that can be solved analytically. We use the analytic solution of each subproblem to approximate the global optimal solution, and enhance the steady-state performance through adaptive adjustment of the penalty parameter.

3.1 Problem Reformulation

For simplicity of representation, we define

$$\begin{cases} \displaystyle\sum_{d,f,k_1,k_2}^{\Omega_a,K} \triangleq \sum_{(d,f)\in\mathbf{\Omega}_a}\sum_{k_1=1}^{K}\sum_{\substack{k_2=1\\k_2=k_1}}^{K} \\ \displaystyle\sum_{d,f,k_1,k_2}^{\Omega_c,K} \triangleq \sum_{(d,f)\in\mathbf{\Omega}_c}\sum_{k_1=1}^{K}\sum_{\substack{k_2=1\\k_2=k_1}}^{K} \end{cases}, \quad (29)$$

To better decompose the original problem, (21) can be rewritten as

$$\begin{aligned} \mathrm{WISL}(\mathbf{s},\mathbf{h}) &= \sum_{d,f,k_1,k_2}^{\Omega_a,K}\left|\mathbf{h}^{\mathrm{H}}\mathbf{Z}_{k_2}^{\mathrm{H}}\mathbf{J}_d\mathbf{D}_f\mathbf{Z}_{k_1}\mathbf{s}\right|^2 \\ &\quad + \sum_{d,f,k_1,k_2}^{\Omega_c,K}\left|\mathbf{h}^{\mathrm{H}}\mathbf{Z}_{k_2}^{\mathrm{H}}\mathbf{J}_d\mathbf{D}_f\mathbf{Z}_{k_1}\mathbf{s}\right|^2 \\ &= \sum_{d,f,k_1,k_2}^{\Omega_a,K}\left|\mathbf{h}^{\mathrm{H}}\mathbf{P}_{k_1,k_2}^{(d,f)}\mathbf{s}\right|^2 \\ &\quad + \sum_{d,f,k_1,k_2}^{\Omega_c,K}\left|\mathbf{h}^{\mathrm{H}}\mathbf{P}_{k_1,k_2}^{(d,f)}\mathbf{s}\right|^2 \end{aligned}, \quad (30)$$

where

$$\begin{cases} \mathbf{Z}_{k_1} = \mathbf{e}_{k_1}^{\top} \otimes \mathbf{I}_L \\ \mathbf{Z}_{k_2} = \mathbf{e}_{k_2}^{\top} \otimes \mathbf{I}_L \end{cases}, \tag{31}$$

$\mathbf{e}_k$ is the k-th standard basis vector and $\mathbf{P}_{k_1,k_2}^{(d,f)} = \mathbf{Z}_{k_2}^{\mathrm{H}} \mathbf{J}_d \mathbf{D}_f \mathbf{Z}_{k_1}$. Accordingly, (26) can be rewritten as

$$\begin{aligned} \mathrm{PL}(\mathbf{s}_k, \mathbf{h}_k) &= \left| \mathbf{h}^{\mathrm{H}} \mathbf{Z}_k^{\mathrm{H}} \mathbf{Z}_k \mathbf{s} - P_m \right|^2 \\ &= \left| \mathbf{h}^{\mathrm{H}} \mathbf{Q}_k \mathbf{s} - P_m \right|^2, \end{aligned} \tag{32}$$

where $\mathbf{Q}_k = \mathbf{Z}_k^{\mathrm{H}} \mathbf{Z}_k$.

The PAPR constraint (27) can be rewritten as

$$\mathbf{s}_k^{\mathrm{H}} \mathbf{E}_{l,k} \mathbf{s}_k \leqslant \rho, l = 1, 2, \ldots, L, \tag{33}$$

where $\mathbf{E}_{l,k}(i,j)$ is defined as

$$\mathbf{E}_{l,k}(i,j) = \begin{cases} 1, & i = l, j = l \\ 0, & \text{otherwise} \end{cases}. \tag{34}$$

Obviously, after the equivalent transformation, (28) has been transformed to the quadratic optimization problem. By using the variable splitting trick and introducing auxiliary variables $\mathbf{m}$, $\mathbf{n}$, $\mathbf{u}$, $\{v_k\}$ and $\mathbf{w}$, the optimization problem in (28) is recast by

$$\begin{aligned} \min_{\mathbf{s},\mathbf{h},\mathbf{m},\mathbf{n},\mathbf{u},\{v_k\},\mathbf{w}} \quad & \mathrm{WISL}(\mathbf{s}, \mathbf{h}) \\ \text{s.t.} \quad & \mathbf{m} = \mathbf{s}, \\ & \|\mathbf{m}_k\|^2 = \mathcal{E}, \\ & \mathbf{n} = \mathbf{h}, \\ & \|\mathbf{n}_k\|^2 = \mathcal{H}, \\ & \mathbf{u} = \mathbf{s}, \\ & \mathbf{u}_k^{\mathrm{H}} \mathbf{E}_{l,k} \mathbf{u}_k \leqslant \rho, \\ & v_k = \mathbf{h}^{\mathrm{H}} \mathbf{Q}_k \mathbf{s} - P_m, \\ & |v_k|^2 \leqslant \theta, \\ & \mathbf{w} = \mathbf{H}\mathbf{s} - \mathbf{x}, \\ & \|\mathbf{w}\|^2 \leqslant \epsilon, \end{aligned} \tag{35}$$

where $k = 1, 2, \ldots, K$.

To improve numerical stability and computational efficiency, we adopt the scaled augmented Lagrangian function of (35), given by

$$\begin{aligned} & L_\mu \left(\mathbf{s}, \mathbf{h}, \mathbf{m}, \mathbf{n}, \mathbf{u}, \{v_k\}, \mathbf{w}, \mathbf{a}, \mathbf{b}, \mathbf{c}, \{d_k\}, \mathbf{e}\right) \\ &= \mathrm{WISL}(\mathbf{s}, \mathbf{h}) + \frac{\mu}{2} \left(\|\mathbf{m} - \mathbf{s} + \mathbf{a}\|^2 - \|\mathbf{a}\|^2\right) \\ &\quad + \frac{\mu}{2} \left(\|\mathbf{n} - \mathbf{h} + \mathbf{b}\|^2 - \|\mathbf{b}\|^2\right) \\ &\quad + \frac{\mu}{2} \left(\|\mathbf{u} - \mathbf{s} + \mathbf{c}\|^2 - \|\mathbf{c}\|^2\right) \\ &\quad + \frac{\mu}{2} \left[\sum_{k=1}^{K} \left(\left|v_k - \mathbf{h}^{\mathrm{H}} \mathbf{Q}_k \mathbf{s} + P_m + d_k\right|^2 - |d_k|^2\right)\right] \\ &\quad + \frac{\mu}{2} \left(\|\mathbf{w} - \mathbf{H}\mathbf{s} + \mathbf{x} + \mathbf{e}\|^2 - \|\mathbf{e}\|^2\right), \end{aligned} \tag{36}$$

where μ is the penalty parameter, $\mathbf{a}$, $\mathbf{b}$, $\mathbf{c}$, $\{d_k\}$ and $\mathbf{e}$ are the dual variables associated with the constraints in (35).

For the above multi-variable optimization problem, we propose the analytic subproblem decomposition (ASD) algorithm, which decomposes the original problem into multiple single-variable subproblems, and each decomposed subproblem can obtain an analytic solution. In the $(t+1)$-th iteration of the proposed method, the solutions of the subproblems can be expressed as

$$\begin{aligned} \mathbf{s}^{t+1} = \arg\min_{\mathbf{s}} L_\mu \big(&\mathbf{s}, \mathbf{h}^t, \mathbf{m}^t, \mathbf{n}^t, \mathbf{u}^t, \{v_k^t\}, \\ &\mathbf{w}^t, \mathbf{a}^t, \mathbf{b}^t, \mathbf{c}^t, \{d_k^t\}, \mathbf{e}^t\big), \end{aligned} \tag{37}$$

$$\begin{aligned} \mathbf{h}^{t+1} = \arg\min_{\mathbf{h}} L_\mu \big(&\mathbf{s}^{t+1}, \mathbf{h}, \mathbf{m}^t, \mathbf{n}^t, \mathbf{u}^t, \{v_k^t\}, \\ &\mathbf{w}^t, \mathbf{a}^t, \mathbf{b}^t, \mathbf{c}^t, \{d_k^t\}, \mathbf{e}^t\big), \end{aligned} \tag{38}$$

$$\begin{aligned} \mathbf{m}^{t+1} = \arg\min_{\mathbf{m}} L_\mu \big(&\mathbf{s}^{t+1}, \mathbf{h}^{t+1}, \mathbf{m}, \mathbf{n}^t, \mathbf{u}^t, \{v_k^t\}, \\ &\mathbf{w}^t, \mathbf{a}^t, \mathbf{b}^t, \mathbf{c}^t, \{d_k^t\}, \mathbf{e}^t\big), \end{aligned} \tag{39}$$

$$\begin{aligned} \mathbf{n}^{t+1} = \arg\min_{\mathbf{n}} L_\mu \big(&\mathbf{s}^{t+1}, \mathbf{h}^{t+1}, \mathbf{m}^{t+1}, \mathbf{n}, \mathbf{u}^t, \{v_k^t\}, \\ &\mathbf{w}^t, \mathbf{a}^t, \mathbf{b}^t, \mathbf{c}^t, \{d_k^t\}, \mathbf{e}^t\big), \end{aligned} \tag{40}$$

$$\begin{aligned} \mathbf{u}^{t+1} = \arg\min_{\mathbf{u}} L_\mu \big(&\mathbf{s}^{t+1}, \mathbf{h}^{t+1}, \mathbf{m}^{t+1}, \mathbf{n}^{t+1}, \mathbf{u}, \\ &\{v_k^t\}, \mathbf{w}^t, \mathbf{a}^t, \mathbf{b}^t, \mathbf{c}^t, \{d_k^t\}, \mathbf{e}^t\big), \end{aligned} \tag{41}$$

$$\begin{aligned} v_k^{t+1} = \arg\min_{v_k} L_\mu \big(&\mathbf{s}^{t+1}, \mathbf{h}^{t+1}, \mathbf{m}^{t+1}, \mathbf{n}^{t+1}, \mathbf{u}^{t+1}, \\ &\{v_k\}, \mathbf{w}^t, \mathbf{a}^t, \mathbf{b}^t, \mathbf{c}^t, \{d_k^t\}, \mathbf{e}^t\big), \end{aligned} \tag{42}$$

$$\begin{aligned} \mathbf{w}^{t+1} = \arg\min_{\mathbf{w}} L_\mu \big(&\mathbf{s}^{t+1}, \mathbf{h}^{t+1}, \mathbf{m}^{t+1}, \mathbf{n}^{t+1}, \mathbf{u}^{t+1}, \\ &\{v_k^{t+1}\}, \mathbf{w}, \mathbf{a}^t, \mathbf{b}^t, \mathbf{c}^t, \{d_k^t\}, \mathbf{e}^t\big), \end{aligned} \tag{43}$$

and the dual variables are updated by

$$\mathbf{a}^{t+1} = \mathbf{m}^{t+1} - \mathbf{s}^{t+1} + \mathbf{a}^t, \tag{44}$$

$$\mathbf{b}^{t+1} = \mathbf{n}^{t+1} - \mathbf{h}^{t+1} + \mathbf{b}^t, \tag{45}$$

$$\mathbf{c}^{t+1} = \mathbf{u}^{t+1} - \mathbf{s}^{t+1} + \mathbf{c}^t, \tag{46}$$

$$d_k^{t+1} = v_k^{t+1} - \left(\mathbf{h}^{t+1}\right)^{\mathrm{H}} \mathbf{Q}_k \mathbf{s}^{t+1} + P_m + d_k^t, \tag{47}$$

$$\mathbf{e}^{t+1} = \mathbf{w}^{t+1} - \mathbf{H}\mathbf{s}^{t+1} + \mathbf{x} + \mathbf{e}^t. \tag{48}$$

3.2 Analytic Solutions to Subproblems

According to the characteristics of each subproblem, we derive their analytic solutions.

3.2.1 Solution to (37)

With fixed $\mathbf{h}^t$, $\mathbf{m}^t$, $\mathbf{n}^t$, $\mathbf{u}^t$, $\{v_k^t\}$ and $\mathbf{w}^t$, the subproblem with respect to $\mathbf{s}$ is a convex quadratic optimization problem. To solve (37), we need to derive its gradient, abbreviated as $\nabla_{\mathbf{s}} L_\mu$, which is expressed as

$$\begin{aligned}\nabla_{\mathbf{s}} L_\mu = 2\mathbf{A}\mathbf{s} &- \mu\left(\mathbf{m}^t - \mathbf{s} + \mathbf{a}^t\right)\\ &- \mu\left(\mathbf{u}^t - \mathbf{s} + \mathbf{c}^t\right)\\ &+ \mu\left[\sum_{k=1}^{K}\left(\mathbf{B}_k\mathbf{s} - p_k\mathbf{Q}_k^{\mathrm{H}}\mathbf{h}^t\right)\right]\\ &- \mu\mathbf{H}^{\mathrm{H}}\left(\mathbf{w}^t - \mathbf{H}\mathbf{s} + \mathbf{x} + \mathbf{e}^t\right),\end{aligned} \tag{49}$$

where

$$\begin{cases}\mathbf{A} = \displaystyle\sum_{d,f,k_1,k_2}^{\Omega_a,K}\left((\mathbf{h}^t)^{\mathrm{H}}\mathbf{P}_{k_1,k_2}^{(d,f)}\right)^{\mathrm{H}}\left((\mathbf{h}^t)^{\mathrm{H}}\mathbf{P}_{k_1,k_2}^{(d,f)}\right),\\ \quad + \displaystyle\sum_{d,f,k_1,k_2}^{\Omega_c,K}\left((\mathbf{h}^t)^{\mathrm{H}}\mathbf{P}_{k_1,k_2}^{(d,f)}\right)^{\mathrm{H}}\left((\mathbf{h}^t)^{\mathrm{H}}\mathbf{P}_{k_1,k_2}^{(d,f)}\right),\\ \mathbf{B}_k = \left((\mathbf{h}^t)^{\mathrm{H}}\mathbf{Q}_k\right)^{\mathrm{H}}(\mathbf{h}^t)^{\mathrm{H}}\mathbf{Q}_k,\\ p_k = v_k^t + P_m + d_k^t.\end{cases} \tag{50}$$

Since $\nabla_{\mathbf{s}} L_\mu$ is linear, by setting $\nabla_{\mathbf{s}} L_\mu = 0$, an analytic solution for (37) can be obtained

$$\mathbf{s}^{t+1} = \boldsymbol{\Gamma}^{-1}\xi, \tag{51}$$

where

$$\boldsymbol{\Gamma} = 2\mathbf{A} + 2\mu\mathbf{I} + \mu\left(\sum_{k=1}^{K}\mathbf{B}_k\right) + \mu\mathbf{H}^{\mathrm{H}}\mathbf{H}, \tag{52}$$

$$\begin{aligned}\xi = \mu\left(\mathbf{m}^t + \mathbf{a}^t\right) + \mu\left(\mathbf{u}^t + \mathbf{c}^t\right) + \mu\left(\sum_{k=1}^{K}p_k\mathbf{Q}_k^{\mathrm{H}}\right)\mathbf{h}^t\\ + \mu\mathbf{H}^{\mathrm{H}}\left(\mathbf{w}^t + \mathbf{x} + \mathbf{e}^t\right).\end{aligned} \tag{53}$$

3.2.2 Solution to (38)

With fixed $\mathbf{s}^{t+1}$, $\mathbf{m}^t$, $\mathbf{n}^t$, $\mathbf{u}^t$, $\{v_k^t\}$ and $\mathbf{w}^t$, the subproblem with respect to $\mathbf{h}$ is also a convex quadratic optimization problem. To solve (38), we need to derive its gradient, abbreviated as $\nabla_{\mathbf{h}} L_\mu$, which is expressed as

$$\begin{aligned}\nabla_{\mathbf{h}} L_\mu = 2\mathbf{C}\mathbf{h} &- \mu\left(\mathbf{n}^t - \mathbf{h} + \mathbf{b}^t\right)\\ &+ \mu\left[\sum_{k=1}^{K}\left(\mathbf{E}_k\mathbf{h} - p_k^*\mathbf{Q}_k\mathbf{s}^{t+1}\right)\right],\end{aligned} \tag{54}$$

where

$$\begin{cases}\mathbf{C} = \displaystyle\sum_{d,f,k_1,k_2}^{\Omega_a,K}\left(\mathbf{P}_{k_1,k_2}^{(d,f)}\mathbf{s}^{t+1}\right)\left(\mathbf{P}_{k_1,k_2}^{(d,f)}\mathbf{s}^{t+1}\right)^{\mathrm{H}},\\ \quad + \displaystyle\sum_{d,f,k_1,k_2}^{\Omega_c,K}\left(\mathbf{P}_{k_1,k_2}^{(d,f)}\mathbf{s}^{t+1}\right)\left(\mathbf{P}_{k_1,k_2}^{(d,f)}\mathbf{s}^{t+1}\right)^{\mathrm{H}},\\ \mathbf{E}_k = \left(\mathbf{Q}_k\mathbf{s}^{t+1}\right)\left(\mathbf{Q}_k\mathbf{s}^{t+1}\right)^{\mathrm{H}},\\ p_k = v_k^t + P_m + d_k^t.\end{cases} \tag{55}$$

Since $\nabla_{\mathbf{h}} L_\mu$ is linear, by setting $\nabla_{\mathbf{h}} L_\mu = 0$, an analytic solution for (38) can be obtained

$$\mathbf{h}^{t+1} = \boldsymbol{\Phi}^{-1}\zeta, \tag{56}$$

where

$$\boldsymbol{\Phi} = 2\mathbf{C} + \mu\mathbf{I} + \mu\left(\sum_{k=1}^{K}\mathbf{E}_k\right), \tag{57}$$

$$\zeta = \mu\left(\mathbf{n}^t + \mathbf{b}^t\right) + \mu\left(\sum_{k=1}^{K}p_k^*\mathbf{Q}_k\right)\mathbf{s}^{t+1}. \tag{58}$$

3.2.3 Solution to (39)

With fixed $\mathbf{s}^{t+1}$, $\mathbf{h}^{t+1}$, $\mathbf{n}^t$, $\mathbf{u}^t$, $\{v_k^t\}$ and $\mathbf{w}^t$, we can rewrite (39) as

$$\begin{aligned}&\min_{\mathbf{m}} \|\mathbf{m} - \mathbf{s}^{t+1} + \mathbf{a}^t\|^2,\\ &\text{s.t. } \|\mathbf{m}_k\|^2 = \mathcal{E}, k = 1, 2, \ldots, K.\end{aligned} \tag{59}$$

Since the objective function is convex quadratic and the constraints enforce spherical equalities on each block, the subproblem admits an analytic solution via independent projection of each block onto its corresponding sphere, which is given by

$$\mathbf{m}^{t+1} = \left[\left(\mathbf{m}_1^{t+1}\right)^{\top}, \left(\mathbf{m}_2^{t+1}\right)^{\top}, \ldots, \left(\mathbf{m}_K^{t+1}\right)^{\top}\right]^{\top}, \tag{60}$$

where

$$\mathbf{m}_k^{t+1} = \frac{\sqrt{\mathcal{E}}}{\|\mathbf{s}_k^{t+1} - \mathbf{a}_k^t\|}\left(\mathbf{s}_k^{t+1} - \mathbf{a}_k^t\right). \tag{61}$$

3.2.4 Solution to (40)

With fixed $\mathbf{s}^{t+1}$, $\mathbf{h}^{t+1}$, $\mathbf{m}^{t+1}$, $\mathbf{u}^t$, $\{v_k^t\}$ and $\mathbf{w}^t$, we can rewrite (40) as

$$\begin{aligned}&\min_{\mathbf{n}} \|\mathbf{n} - \mathbf{h}^{t+1} + \mathbf{b}^t\|^2,\\ &\text{s.t. } \|\mathbf{n}_k\|^2 = \mathcal{H}, k = 1, 2, \ldots, K.\end{aligned} \tag{62}$$

Due to the same structure as (59), the subproblem admits the analytic solution

$$\mathbf{n}^{t+1} = \left[\left(\mathbf{n}_1^{t+1}\right)^{\top}, \left(\mathbf{n}_2^{t+1}\right)^{\top}, \ldots, \left(\mathbf{n}_k^{t+1}\right)^{\top}\right]^{\top}, \tag{63}$$

where

$$\mathbf{n}_k^{t+1} = \frac{\sqrt{\mathcal{H}}}{\|\mathbf{h}_k^{t+1} - \mathbf{b}_k^t\|}\left(\mathbf{h}_k^{t+1} - \mathbf{b}_k^t\right). \tag{64}$$

Algorithm 1 The ASD Algorithm to Update Solutions

Input: Initial waveform $\mathbf{s}_r$, initial filter $\mathbf{h}_r$, penalty parameter μ_r, residual tolerance $\eta_{pres} > 0$, $\eta_{dres} > 0$, maximum inner iterations T_{max}.
Set inner iteration number $t = 0$, $\mathbf{s}^0 = \mathbf{s}_r$, $\mathbf{h}^0 = \mathbf{h}_r$, $\mu = \mu_r$;
Initialize primal variables $\mathbf{m}^0 = \mathbf{s}^0$, $\mathbf{n}^0 = \mathbf{h}^0$, $\mathbf{u}^0 = \mathbf{s}^0$, $\{v_k^0\} = \{0\}$ and $\mathbf{w}^0 = \mathbf{0}$, dual variables $\mathbf{a}^0 = \mathbf{0}$, $\mathbf{b}^0 = \mathbf{0}$, $\mathbf{c}^0 = \mathbf{0}$, $\{d_k^0\} = \{0\}$ and $\mathbf{e}^0 = \mathbf{0}$;
Compute $\mathbf{P}_{k_1,k_2}^{(d,f)}$ and $\mathbf{Q}_k$;
repeat
  Update $\mathbf{s}^{t+1}$ by (51);
  Update $\mathbf{h}^{t+1}$ by (56);
  Update $\mathbf{m}^{t+1}$, $\mathbf{n}^{t+1}$, $\mathbf{u}^{t+1}$, $\{v_k^{t+1}\}$ and $\mathbf{w}^{t+1}$ by (60), (63), (66), (69) and (71), respectively;
  Update $\mathbf{a}^{t+1}$, $\mathbf{b}^{t+1}$, $\mathbf{c}^{t+1}$, $\{d_k^{t+1}\}$ and $\mathbf{e}^{t+1}$ by (44), (45), (46), (47) and (48), respectively;
  $t = t + 1$;
until
 $(\mathcal{P}^{t+1} < \eta_{pres}$ and $\mathcal{D}^{t+1} < \eta_{dres})$ or $t > T_{max}$;
Output: $\mathbf{s}_{r+1} = \mathbf{s}^{t+1}$, $\mathbf{h}_{r+1} = \mathbf{h}^{t+1}$, $\mathcal{P}_{r+1} = \mathcal{P}^{t+1}$ and $\mathcal{D}_{r+1} = \mathcal{D}^{t+1}$.

3.2.5 *Solution to* (41)

With fixed $\mathbf{s}^{t+1}$, $\mathbf{h}^{t+1}$, $\mathbf{m}^{t+1}$, $\mathbf{n}^{t+1}$, $\{v_k^t\}$ and $\mathbf{w}^t$, we can rewrite (41) as

$$\begin{aligned} &\min_{\mathbf{u}} \|\mathbf{u} - \mathbf{x}^{t+1} + \mathbf{c}^t\|^2, \\ &\text{s.t. } \mathbf{u}_k^{\mathrm{H}} \mathbf{E}_{l,k} \mathbf{u}_k \leqslant \rho, \\ &\qquad l = 1, 2, \ldots, L, k = 1, 2, \ldots, K. \end{aligned} \tag{65}$$

By using Lagrange duality and Karush-Kuhn-Tucker (KKT) conditions, we define $\mathbf{f}_k = \mathbf{x}_k^{t+1} - \mathbf{c}_k^t$ and the analytic solution is given by

$$\mathbf{u}^{t+1} = \left[\left(\mathbf{u}_1^{t+1}\right)^\top, \left(\mathbf{u}_2^{t+1}\right)^\top, \ldots, \left(\mathbf{u}_K^{t+1}\right)^\top \right]^\top, \tag{66}$$

where

$$\mathbf{u}_k^{t+1}(l) = \begin{cases} \mathbf{f}_k(l), & |\mathbf{f}_k(l)|^2 \leqslant \rho, \\ \dfrac{\sqrt{\rho}}{|\mathbf{f}_k(l)|} \mathbf{f}_k(l), & |\mathbf{f}_k(l)|^2 > \rho. \end{cases} \tag{67}$$

3.2.6 *Solution to* (42)

With fixed $\mathbf{s}^{t+1}$, $\mathbf{h}^{t+1}$, $\mathbf{m}^{t+1}$, $\mathbf{n}^{t+1}$, $\mathbf{u}^{t+1}$ and $\mathbf{w}^t$, we define $\beta_k = \left(\mathbf{h}^{t+1}\right)^{\mathrm{H}} \mathbf{Q}_k \mathbf{s}^{t+1} - P_m - d_k^t$ and (42) can be rewritten as

$$\begin{aligned} &\min_{v_k} \ |v_k - \beta_k|^2, \\ &\text{s.t. } |v_k|^2 \leqslant \theta, k = 1, 2, \ldots, K. \end{aligned} \tag{68}$$

which is a constrained least squares problem and the analytic solution is given by

$$v_k^{t+1} = \begin{cases} \beta_k, & |\beta_k|^2 \leqslant \theta, \\ \sqrt{\theta}, & |\beta_k|^2 > \theta. \end{cases} \tag{69}$$

3.2.7 *Solution to* (43)

With fixed $\mathbf{s}^{t+1}$, $\mathbf{h}^{t+1}$, $\mathbf{m}^{t+1}$, $\mathbf{n}^{t+1}$, $\mathbf{u}^t$ and $\{v_k^{t+1}\}$, we define $\mathbf{g} = \mathbf{H}\mathbf{s}^{t+1} - \mathbf{x} - \mathbf{e}^t$ and (43) can be rewritten as

$$\begin{aligned} &\min_{\mathbf{w}} \|\mathbf{w} - \mathbf{g}\|^2, \\ &\text{s.t. } \|\mathbf{w}\|^2 \leqslant \epsilon. \end{aligned} \tag{70}$$

This is equivalent to the problem in (68), and its analytic solution is given by

$$\mathbf{w}^{t+1} = \begin{cases} \mathbf{g}, & \|\mathbf{g}\|^2 \leqslant \epsilon, \\ \dfrac{\sqrt{\epsilon}}{\|\mathbf{g}\|} \mathbf{g}, & \|\mathbf{g}\|^2 > \epsilon. \end{cases} \tag{71}$$

In summary, the ASD algorithm for updating solutions is summarized in **Algorithm 1**, where we stop the proposed algorithm when the primal residual $\mathcal{P}^t \leqslant \eta_{pres}$ and the dual residual $\mathcal{D}^t \leqslant \eta_{dres}$, where

$$\begin{aligned} \mathcal{P}^t = &\max_{k=1,2,\ldots,K} \Big\{ \|\mathbf{m}^t - \mathbf{s}^t\|, \|\mathbf{n}^t - \mathbf{h}^t\|, \|\mathbf{u}^t - \mathbf{s}^t\|, \\ &|v_k^t - \left(\mathbf{h}^t\right)^{\mathrm{H}} \mathbf{Q}_k \mathbf{s}^t + P_m|, \|\mathbf{w}^t - \mathbf{H}\mathbf{s}^t + \mathbf{x}\| \Big\}, \end{aligned} \tag{72}$$

$$\begin{aligned} \mathcal{D}^t = &\max_{k=1,2,\ldots,K} \Big\{ \|\mathbf{s}^t - \mathbf{s}^{t-1}\|, \|\mathbf{h}^t - \mathbf{h}^{t-1}\|, \\ &\|\mathbf{m}^t - \mathbf{m}^{t-1}\|, \|\mathbf{n}^t - \mathbf{n}^{t-1}\|, \|\mathbf{u}^t - \mathbf{u}^{t-1}\|, \\ &|v_k^t - v_k^{t-1}|, \|\mathbf{w}^t - \mathbf{w}^{t-1}\| \Big\}, \end{aligned} \tag{73}$$

where $\eta_{pres} > 0$ and $\eta_{dres} > 0$ are the feasible tolerances of the primal and dual conditions, respectively.

3.3 Update the Penalty Parameter

The penalty parameter μ plays a key role in controlling the strictness of constraint enforcement, balancing the updates of primal and dual variables, and influencing the convergence speed and stability of the algorithm. To prevent large discrepancies between the updates of the primal and dual variables in the proposed algorithm, it is necessary to adjust the penalty parameter accordingly, where

$$\mu_{r+1} = \begin{cases} \kappa_{incr} \mu_r, & if\ \mathcal{P}_r > \psi \mathcal{D}_r, \\ \mu_r / \kappa_{decr}, & if\ \mathcal{D}_r > \psi \mathcal{P}_r, \\ \mu_r, & else. \end{cases} \tag{74}$$

where κ_{incr} and κ_{decr} are the increase and decrease scaling factor, respectively, ψ is the residual balance parameter. To ensure convergence, the penalty parameter is constrained within predefined bounds, preventing it from becoming unreasonably small or large during iterations, denoted as $\mu \in [\mu_{min}, \mu_{max}]$.

Algorithm 2 The APASD Framework for Solving (35)

Input: Initial waveform $\mathbf{s}_0$, initial filter $\mathbf{h}_0$, penalty parameter μ_0, minimum step size γ, maximum outer iterations R_{max}.
Set outer iteration number $r = 0$;
repeat
  Update $\mathbf{s}_{r+1}$ and $\mathbf{h}_{r+1}$ by **Algorithm 1**;
  Obtain $\mathcal{P}_{r+1}$ and $\mathcal{D}_{r+1}$ by **Algorithm 1**;
  if $\mathcal{P}_{r+1} > \psi\mathcal{D}_{r+1}$ **then**
    $\mu_{r+1} = \min\{\kappa_{incr}\mu_r, \mu_{max}\}$;
  else if $\mathcal{D}_{r+1} > \psi\mathcal{P}_{r+1}$ **then**
    $\mu_{r+1} = \max\{\mu_r/\kappa_{decr}, \mu_{min}\}$;
  else
    $\mu_{r+1} = \mu_r$;
  end if
  $r = r + 1$;
until $\max\{\|\mathbf{s}_{r+1} - \mathbf{s}_r\|, \|\mathbf{h}_{r+1} - \mathbf{h}_r\|\} < \gamma$ or $r > R_{max}$;
Output: Optimal $\mathbf{s}_{opt} = \mathbf{s}_{r+1}$ and $\mathbf{h}_{opt} = \mathbf{h}_{r+1}$.

For stable penalty parameter updates, adjustments are performed only after the completion of each inner loop. We summarize the proposed APASD framework in **Algorithm 2** and the termination condition is defined by the minimum step size threshold and denoted by γ.

3.4 Computational Complexity Analysis

The overall computational complexity of the proposed method are linear with the number of iterations. In each iteration, the complexity is approximately $\mathcal{O}(L^3K^3 + L^3K^2U + L^2K^2 + L^2KU)$, which is primarily attributed to the update steps for $\mathbf{s}$ in (37) and $\mathbf{h}$ in (38). The main computational complexity of the ADMM [26] and Method [25] are the same as that of the proposed method.

4 Numerical Results

In this section, numerical results are provided to demonstrate the performance of the proposed method. Without loss of generality, we consider the state-of-the-art ADMM [26] and Method [25] for comparison. In addition, we also consider the performance of the proposed method at low PAPR and its convergence behaviors.

We define the normalized AF (NAF), which consists of the normalized AAF (NAAF) and the normalized CAF (NCAF), to evaluate the correlation performance of the waveform [42].

$$\mathrm{NAAF} = 20\log_{10}\frac{|\mathrm{AF}_{k_1,k_2}(d,f)|}{\|\mathbf{h}_{k_2}\|\|\mathbf{s}_{k_1}\|},$$

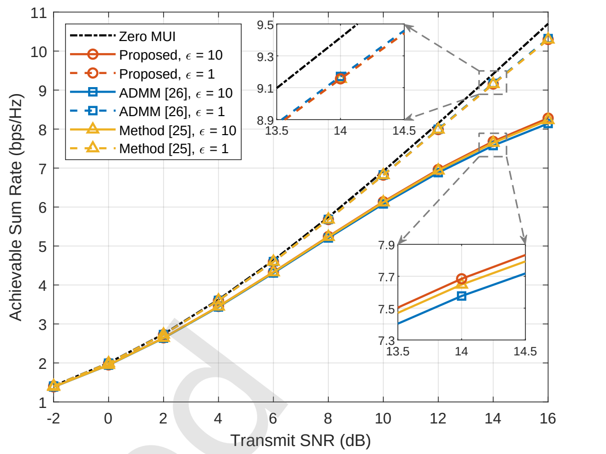

Fig. 2 The achievable sum-rate versus the transmit SNR for different ϵ.

$$k_1, k_2 = 1, 2, \ldots, K \; and \; k_1 = k_2 \tag{75}$$

$$\mathrm{NCAF} = 20\log_{10}\frac{|\mathrm{AF}_{k_1,k_2}(d,f)|}{\|\mathbf{h}_{k_2}\|\|\mathbf{s}_{k_1}\|},$$
$$k_1, k_2 = 1, 2, \ldots, K \; and \; k_1 \neq k_2 \tag{76}$$

The simulation parameters are set as follows: $M = 8, N = 16, L = MN = 128$, the number of transmit antennas $K = 4$, the number of users $U = 2$, the energy of the transmitted waveform $\mathcal{E} = L$, the energy of the mismatched filter $\mathcal{H} = L$, the interested region of AAF $\mathbf{\Omega}_a = \{(d,f) \mid d = -3,\ldots,3; f = -2,\ldots,2\}$ and the interested region of CAF $\mathbf{\Omega}_c = \{(d,f) \mid d = -3,\ldots,3; f = -2,\ldots,2\}$, the false alarm probability $P_{FA} = 10^{-6}$, and the strong clutter interference region corresponds to the interested region in the AF plane.

Within the proposed APASD framework, we define $\mu_0 = 100$, $\psi = 10$, $\kappa_{incr} = 1.5$, $\kappa_{decr} = 1.5$, $\mu_{max} = 400$, $\mu_{min} = 20$, $\eta_{pres} = 10^{-4}$, $\eta_{dres} = 10^{-4}$, $\gamma = 10^{-6}$, $T_{max} = 20$ and $R_{max} = 300$.

We conducted our experiments using MATLAB 2023b on a standard PC with the following specifications: Intel Core i5-12400F processor, NVIDIA RTX 3060 GPU, 512GB SSD, and 1TB HDD.

4.1 Performance Comparison

In this experiment, we set $\rho = 2, \theta = 1$, and ϵ was sequentially set to 10 and 1, with a 1 dB SNR loss due to mismatched filtering. The ADMM [26] and Method [25] are used as the comparison and adopt the same iteration termination criterion as the proposed method.

Fig. 2 shows the achievable sum-rate versus the transmit SNR for different ϵ. As can be seen, the achievable sum-rate becomes higher when we decrease ϵ, indicating better

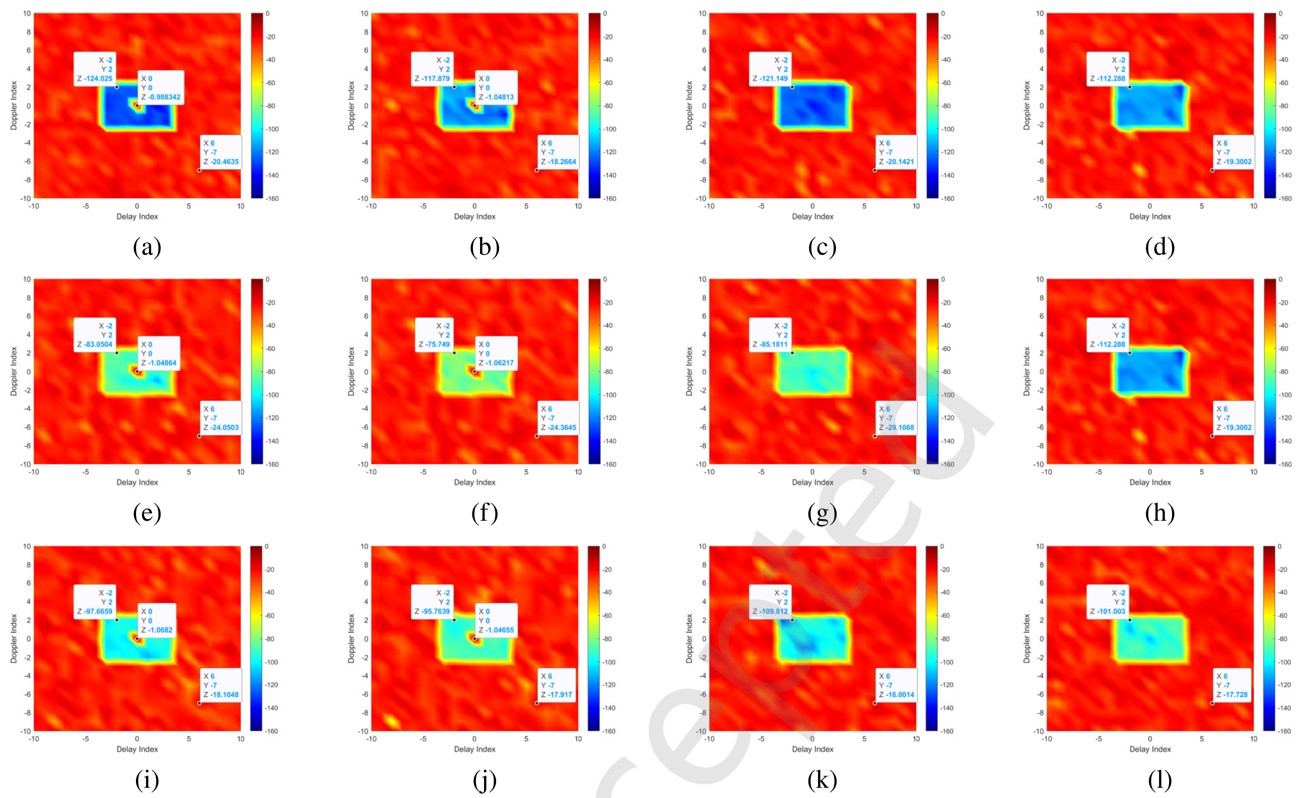

Fig. 3 NAFs under different MUI energy thresholds. (a) The NAAF of the proposed method, $\epsilon = 10$. (b) The NAAF of the proposed method, $\epsilon = 1$. (c) The NCAF of the proposed method, $\epsilon = 10$. (d) The NCAF of the proposed method, $\epsilon = 1$. (e) The NAAF of ADMM [26], $\epsilon = 10$. (f) The NAAF of ADMM [26], $\epsilon = 1$. (g) The NCAF of ADMM [26], $\epsilon = 10$. (h) The NCAF of ADMM [26], $\epsilon = 1$. (i) The NAAF of Method [25], $\epsilon = 10$. (j) The NAAF of Method [25], $\epsilon = 1$. (k) The NCAF of Method [25], $\epsilon = 10$. (l) The NCAF of Method [25], $\epsilon = 1$.

communication performance. The three methods have similar communication performance under the same MUI energy threshold.

Fig. 3 shows the comparison of the NAFs under different MUI energy thresholds. As can be seen, the nulls in the interested region are deeper when we increase ϵ, which means the better sensing performance. However, the communication performance correspondingly degrades, as shown in Fig. 2. By decomposing the original problem into multiple subproblems that can be solved analytically, the proposed method achieves superior performance. The proposed method can form about 30 dB deeper nulls compared to ADMM [26] and 10 dB deeper nulls compared to Method [25], indicating better sensing performance.

Fig. 4 and Fig. 5 present the Delay-cut plots of NAAF and NCAF, respectively, at $d = 0$. The proposed method yields an average sensing gain of approximately 30 dB over the ADMM [26] and 10 dB over Method [25] across the evaluated range of ϵ.

Fig. 6 shows the comparison of the weak target detection probability when $\epsilon = 1$. As can be seen, against strong

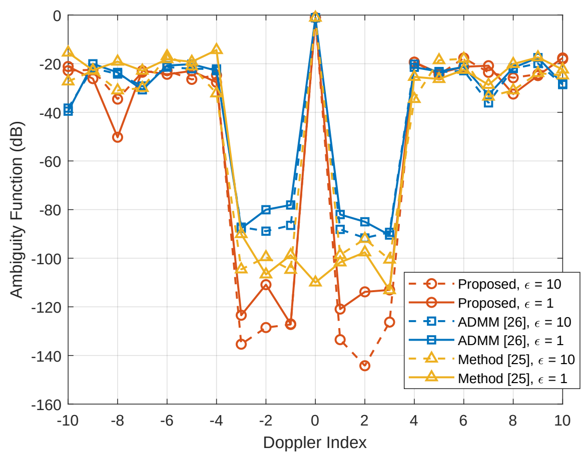

Fig. 4 Delay-cut of NAAFs when $d = 0$.

clutter backgrounds, the proposed method achieves better target detection performance than ADMM [26] and Method [25] under the same transmit SNR. Moreover, as the clutter intensity increases, the advantage of the proposed method becomes more pronounced.

Table 2 shows the comparison of convergence behavior

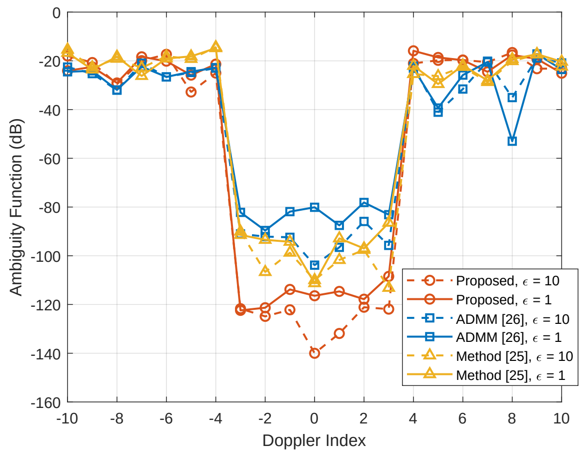

Fig. 5 Delay-cut of NCAFs when $d = 0$.

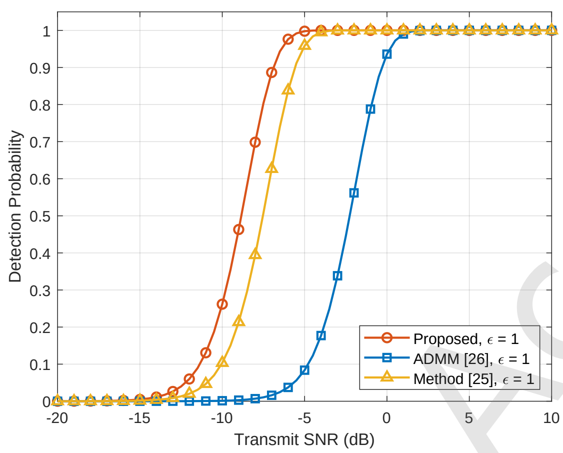

Fig. 6 The weak target detection probability versus the transmit SNR when $\epsilon = 1$.

when $\epsilon = 1$. It can be seen that, the designed waveforms by all methods satisfy all constraints. Furthermore, compared with the other two methods, the proposed method achieves lower sidelobe levels in the designed waveforms upon convergence, and its running time is shorter.

Table 2 Comparison of convergence behavior when $\epsilon = 1$.

Methods	Constraints Satisfaction	WISL (dB)	Time (s)
Proposed	Yes	**-26.4**	**30.7**
ADMM [26]	Yes	-9.7	58.1
Method [25]	Yes	-17.2	38.6

4.2 Low PAPR Performance

We conducted experiments to evaluate the impact of introducing a mismatched filter on the design of low PAPR waveforms.

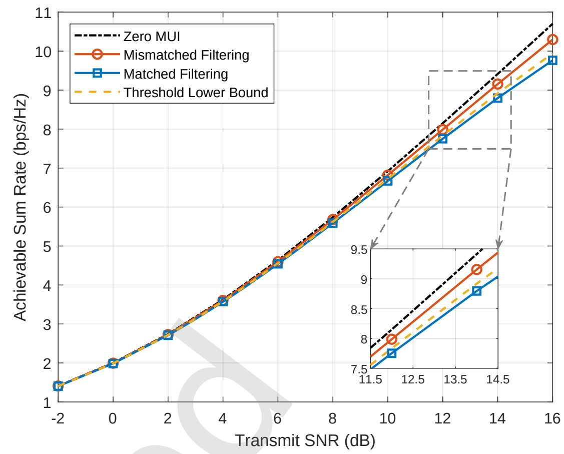

Fig. 7 The achievable sum-rate versus the transmit SNR for mismatched and matched filter.

For comparison, the proposed method was applied to a problem model employing matched filtering in the sensing module, thereby transforming (28) into a single variable problem with respect to s. Throughout the experiments, a low PAPR threshold of $\rho = 1.5$ was imposed, with the other parameters set to $\epsilon = 1$ and $\theta = 1$. In this case, mismatched filtering incurred a 1 dB peak SNR loss.

Fig. 7 shows the achievable sum-rate versus the transmit SNR for mismatched and matched filter. As illustrated, when the PAPR threshold is equal to 1.5, the achievable sum-rate under mismatched filtering can meet the minimum threshold requirement, but matched filtering cannot, which means that mismatched filtering has better communication performance at low PAPR.

In Fig. 8, the NAAF and NCAF under mismatched and matched filtering are presented. As can be seen, under a low PAPR condition, matched filtering fails to form deep nulls in the region of interest without compromising communication performance, thus failing to achieve the desired sensing performance. In contrast, mismatched filtering successfully forms deep nulls under the same conditions, demonstrating robust sensing capability.

In summary, under low PAPR, mismatched filtering, although incurring a certain peak SNR loss, achieves improved communication and sensing performance.

4.3 Convergence Behaviors

In this subsection, we evaluate the convergence behaviors of the proposed method. To allow the objective function to sufficiently decrease until convergence, the restriction on the residual tolerances are lifted, and sufficient iterations are ensured.

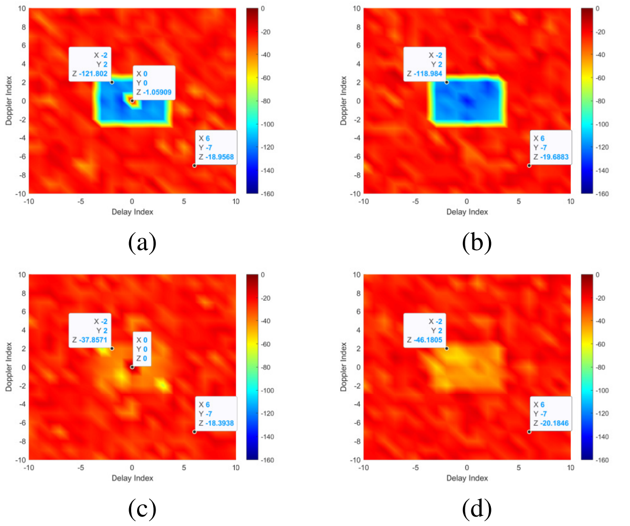

Fig. 8 NAFs under mismatched and matched filtering when $\epsilon = 1$. (a) The NAAF of mismatched filtering. (b) The NCAF of mismatched filtering. (c) The NAAF of matched filtering. (d) The NCAF of matched filtering.

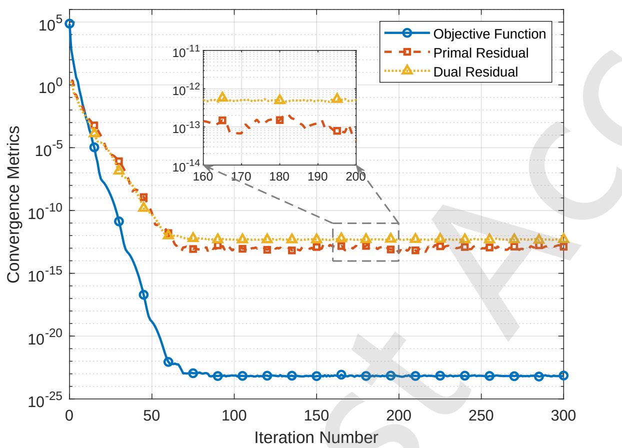

Fig. 9 The convergence metrics versus the iteration number for $\rho = 2$.

In Fig. 9, the objective function, primal residual and dual residual are presented against the iteration number for $\rho = 2$. It is evident that when the objective function curve converges to a fixed value and exhibits minor fluctuations around it, the residual correspondingly converges.

Fig. 10 shows the objective function versus the iteration number for different ρ. As can be seen, a larger PAPR threshold leads to a more significant decrease in the objective function within the same number of iterations and results in faster convergence. Conversely, under strict PAPR constraints, the optimization problem becomes more challenging, which consequently impacts the final convergence value.

Fig. 11 shows the objective function versus the iteration number for adaptive and fixed μ. As can be seen, compared to

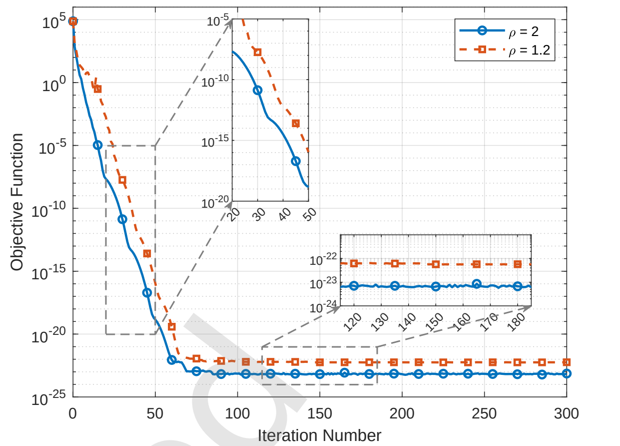

Fig. 10 The objective function versus the iteration number for different ρ.

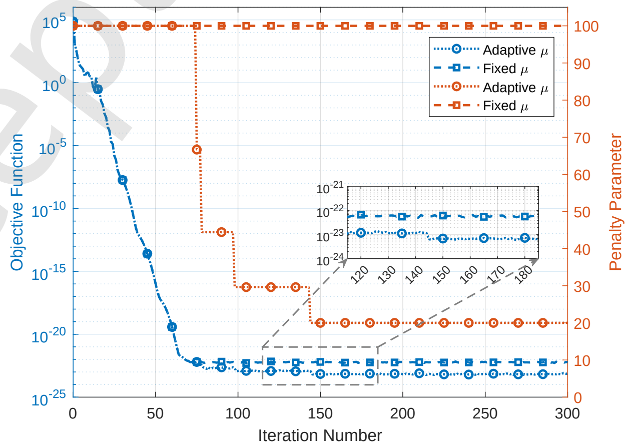

Fig. 11 The objective function versus the iteration number for adaptive and fixed μ.

a fixed μ, adaptively adjusting μ enables the objective function to converge to a smaller value, demonstrating superior ultimate performance. This indicates that dynamically tuning the value of μ can enhance the radar detection performance of the system.

5 Conclusion

In contrast to prior work that focuses on MIMO-OTFS communication or SISO-OTFS dual-functional waveform design, this paper introduces a waveform optimization framework for MIMO-OTFS ISAC systems via WISL minimization under PAPR and MUI energy constraints. The APASD method is introduced to efficiently solve the problem by deriving analytic solutions to decomposed subproblems and updating penalty parameter adaptively. Simulations show the peoposed method achieves lower sidelobe while maintaining communication performance, and delivers superior performance compared with existing methods.

In the future, we will extend the proposed method to the joint optimization of wireless channel estimation and MIMO-OTFS ISAC waveform design.

Appendix

In this appendix, we prove the convergence of **Algorithm 1**. Since the proposed APASD method decomposes the original problem into multiple subproblems, we restate (35) in a more concise form for ease of analysis. Let the primal variables be $\mathbf{y} = \{\mathbf{s}, \mathbf{h}\}$ and the auxiliary variables be $\mathbf{z} = \{\mathbf{m}, \mathbf{n}, \mathbf{u}, \{v_k\}, \mathbf{w}\}$. The problem can then be rewritten as

$$\begin{aligned} &\min_{\mathbf{y},\mathbf{z}} f(\mathbf{y}) + g(\mathbf{z}) \\ &\text{s.t. } \mathbf{z} = \Phi(\mathbf{y}), \end{aligned} \tag{77}$$

where the function $f(\mathbf{y}) = \mathrm{WISL}(\mathbf{s}, \mathbf{h})$ is smooth. The function $g(\mathbf{z})$ is the indicator function $I_{\mathcal{Z}}(\mathbf{z})$ for the compact, non-convex constraint set $\mathcal{Z}$. The indicator function is formally defined as:

$$g(\mathbf{z}) = I_{\mathcal{Z}}(\mathbf{z}) = \begin{cases} 0, & \text{if } \mathbf{z} \in \mathcal{Z} \\ +\infty, & \text{if } \mathbf{z} \notin \mathcal{Z} \end{cases}, \tag{78}$$

and the constraint set $\mathcal{Z}$ is defined as

$$\mathcal{Z} = \left\{ (\mathbf{m}, \mathbf{n}, \mathbf{u}, \{v_k\}, \mathbf{w}) \;\middle|\; \begin{aligned} &\|\mathbf{m}_k\|^2 = \mathcal{E}, \\ &\|\mathbf{n}_k\|^2 = \mathcal{H}, \\ &\mathbf{u}_k^{\mathrm{H}} \mathbf{E}_{l,k} \mathbf{u}_k \leqslant \rho, \\ &|v_k|^2 \leqslant \theta, \\ &\|\mathbf{w}\|^2 \leqslant \epsilon \end{aligned} \right\}. \tag{79}$$

The coupling function $\Phi(\mathbf{y})$ is defined by the system of constraints, which dictates the residual $\mathbf{r} = \Phi(\mathbf{y}) - \mathbf{z}$,

$$\mathbf{z} = \Phi(\mathbf{y}) \iff \begin{cases} \mathbf{m} = \mathbf{s}, \\ \mathbf{n} = \mathbf{h}, \\ \mathbf{u} = \mathbf{s}, \\ v_k = \mathbf{h}^{\mathrm{H}} \mathbf{Q}_k \mathbf{s} - P_m, \\ \mathbf{w} = \mathbf{H}\mathbf{s} - \mathbf{x}. \end{cases} \tag{80}$$

In the t-th iteration, the scaled augmented Lagrangian $\mathcal{L}_\mu$, using the scaled dual variable $\mathbf{k}$, is defined as

$$\begin{aligned} \mathcal{L}_\mu(\mathbf{y}, \mathbf{z}, \mathbf{k}^t) = &f(\mathbf{y}) + g(\mathbf{z}) \\ &+ \frac{\mu}{2} \left(\|\Phi(\mathbf{y}) - \mathbf{z} + \mathbf{k}^t\|^2 - \|\mathbf{k}^t\|^2 \right). \end{aligned} \tag{81}$$

The update for the scaled dual variable is

$$\mathbf{k}^{t+1} = \mathbf{k}^t + (\Phi(\mathbf{y}^{t+1}) - \mathbf{z}^{t+1}) = \mathbf{k}^t + \mathbf{r}^{t+1} \tag{82}$$

The $\mathbf{y}$-update minimizes $\mathcal{L}_\mu(\mathbf{y}, \mathbf{z}^t, \mathbf{k}^t)$. Because $f(\mathbf{y})$ is smooth and μ is chosen large enough, the quadratic penalty term ensures $\mathcal{L}_\mu$ is strongly convex w.r.t. $\mathbf{y}$, yielding a sufficient descent

$$\mathcal{L}_\mu(\mathbf{y}^{t+1}, \mathbf{z}^t, \mathbf{k}^t) \leqslant \mathcal{L}_\mu(\mathbf{y}^t, \mathbf{z}^t, \mathbf{k}^t) - \frac{\gamma}{2}\|\mathbf{y}^{t+1} - \mathbf{y}^t\|^2, \tag{83}$$

where $\gamma > 0$ is the strong convexity modulus. Since each decomposed subproblem has a closed-form solution, the $\mathbf{z}$-update performs an exact minimization of $\mathcal{L}_\mu(\mathbf{y}^{t+1}, \mathbf{z}, \mathbf{k}^t)$, using the newly obtained $\mathbf{y}^{t+1}$ and a non-increasing property is immediate

$$\mathcal{L}_\mu(\mathbf{y}^{t+1}, \mathbf{z}^{t+1}, \mathbf{k}^t) \leqslant \mathcal{L}_\mu(\mathbf{y}^{t+1}, \mathbf{z}^t, \mathbf{k}^t). \tag{84}$$

The dual update introduces a change in the Lagrangian exactly proportional to the squared residual $\mathbf{r}^{t+1}$, as $\mathbf{k}^{t+1} = \mathbf{k}^t + \mathbf{r}^{t+1}$,

$$\mathcal{L}_\mu(\mathbf{y}^{t+1}, \mathbf{z}^{t+1}, \mathbf{k}^{t+1}) = \mathcal{L}_\mu(\mathbf{y}^{t+1}, \mathbf{z}^{t+1}, \mathbf{k}^t) + \mu\|\mathbf{r}^{t+1}\|^2. \tag{85}$$

Based on the smoothness premise and the optimality conditions of the $\mathbf{y}$ and $\mathbf{z}$ updates, the residual term is quadratically bounded by the changes in the variables

$$\mu\|\mathbf{r}^{t+1}\|^2 \leqslant c_1\|\mathbf{y}^{t+1} - \mathbf{y}^t\|^2 + c_2\|\mathbf{z}^{t+1} - \mathbf{z}^t\|^2, \tag{86}$$

where c_1 and c_2 are constants related to μ.

By combining the descent steps (83) and (84) with the ascent step (85) and (86), and ensuring γ is large enough (such that $\frac{\gamma}{2} > c_1$), the strict monotonically decreasing property of the Lyapunov function $\Psi^t = \mathcal{L}_\mu(\mathbf{y}^t, \mathbf{z}^t, \mathbf{k}^t)$ is established

$$\begin{aligned} \mathcal{L}_\mu(\mathbf{y}^{t+1}, \mathbf{z}^{t+1}, \mathbf{k}^{t+1}) \leqslant \mathcal{L}_\mu(\mathbf{y}^t, \mathbf{z}^t, \mathbf{k}^t) - \delta \big(&\|\mathbf{y}^{t+1} - \mathbf{y}^t\|^2 \\ &+ \|\mathbf{z}^{t+1} - \mathbf{z}^t\|^2 \big) \end{aligned} \tag{87}$$

for some $\delta > 0$.

Since the objective function is bounded below and the constraint set $\mathcal{Z}$ is compact, the sequence $\{\mathcal{L}_\mu(\mathbf{y}^t, \mathbf{z}^t, \mathbf{k}^t)\}$ is lower-bounded. This monotonically decreasing property ensures the sequence converges, which forces the successive differences and the residual $\mathbf{r}^{t+1}$ to zero

$$\begin{aligned} &\lim_{t\to\infty} \|\mathbf{y}^{t+1} - \mathbf{y}^t\| = 0, \\ &\lim_{t\to\infty} \|\mathbf{z}^{t+1} - \mathbf{z}^t\| = 0, \\ &\lim_{t\to\infty} \|\mathbf{r}^{t+1}\| = 0. \end{aligned} \tag{88}$$

Thus, the sequence generated by the APASD method converges to a KKT stationary point of the problem.

Acknowledgment

This work was supported in part by the National Natural Science Foundation of China under Grants 62231006 and 62501112, the National Key R&D Program of China under Grant 2023YFF0717403, the China Postdoctoral Science Foundation under Grant 2025M773511, and the Municipal Government of Quzhou under Grants 2024D005 and 2025K008.

Declaration of competing interest

The authors have no competing interests to declare that are relevant to the content of this article.

Reference

[1] B. Hu, W. Zhang, Y. Gao, J. Du, and X. Chu, Multiagent deep deterministic policy gradient-based computation offloading and resource allocation for isac-aided 6g v2x networks, *IEEE Internet of Things Journal*, vol. 11, no. 20, pp. 33 890–33 902, 2024.

[2] X. Xi, X. Cao, P. Yang, J. Chen, T. Quek, and D. Wu, Joint user association and uav location optimization for uav-aided communications, *IEEE Wireless Communications Letters*, vol. 8, no. 6, pp. 1688–1691, 2019.

[3] Z. Zhang, H. Ren, C. Pan, S. Hong, D. Wang, J. Wang, and X. You, Target localization in cooperative isac systems: A scheme based on 5g nr ofdm signals, *IEEE Transactions on Communications*, vol. 73, no. 5, pp. 3562–3578, 2025.

[4] K. Zhong, J. Hu, C. Pan, M. Deng, and J. Fang, Joint waveform and beamforming design for ris-aided isac systems, *IEEE Signal Processing Letters*, vol. 30, pp. 165–169, 2023.

[5] Z. Ren, C. Pan, H. Ren, D. Wang, L. Xu, and J. Wang, Two-timescale design for ap mode selection and power allocation of cooperative isac networks, *IEEE Transactions on Wireless Communications*, pp. 1–1, 2025.

[6] B. Liao, H. Q. Ngo, M. Matthaiou, and P. J. Smith, Power allocation for massive mimo-isac systems, *IEEE Transactions on Wireless Communications*, vol. 23, no. 10, pp. 14 232–14 248, 2024.

[7] J. Tang, Y. Yu, C. Pan, H. Ren, D. Wang, J. Wang, and X. You, Cooperative isac-empowered low-altitude economy, *IEEE Transactions on Wireless Communications*, vol. 24, no. 5, pp. 3837–3853, 2025.

[8] D. An, J. Hu, R. Wang, X. Tai, Y. Zuo, K. Zhong, F. Gini, and M. S. Greco, Movable antenna enhanced beampattern synthesis for spectrum constrained mimo radar, *IEEE Transactions on Signal Processing*, vol. 73, pp. 3478–3495, 2025.

[9] V. S. Bhat, S. G. Dayanand, and A. Chockalingam, Performance analysis of otfs modulation with receive antenna selection, *IEEE Transactions on Vehicular Technology*, vol. 70, no. 4, pp. 3382–3395, 2021.

[10] C. Shi, L. Zhao, Y. Cui, Y. Chu, W. Guo, and W. Wang, Joint detection and channel estimation for mimo-otfs systems, *IEEE Transactions on Vehicular Technology*, vol. 73, no. 8, pp. 11 568–11 579, 2024.

[11] S. Qi, Q. Wang, and Z. Ma, Deep residual attention network for otfs channel estimation, *IEEE Transactions on Vehicular Technology*, vol. 74, no. 6, pp. 9834–9839, 2025.

[12] B. Zhang, L. Mei, Z. Li, Z. Du, and E. Basar, Otfs with dual frequency index modulation, *IEEE Transactions on Wireless Communications*, vol. 23, no. 10, pp. 14 910–14 923, 2024.

[13] X. Wang, X. Shi, and J. Wang, Sparse bayesian learning based off-grid estimation of otfs channels with doppler squint, *Tsinghua Science and Technology*, vol. 29, no. 6, pp. 1821–1828, 2024.

[14] Y. Yang, Y. Pan, X. Liu, and M. Peng, Barycenter calibration with high order spectra of windowed delay-doppler signals for otfs based isac systems, *IEEE Transactions on Signal Processing*, vol. 72, pp. 2450–2466, 2024.

[15] M. Jafri, S. Srivastava, and A. K. Jagannatham, Sparse target parameter and channel estimation in mmwave mimo otfs-aided integrated sensing and communication systems, *IEEE Transactions on Communications*, vol. 73, no. 2, pp. 1320–1335, 2025.

[16] X. Xia, K. Xu, Y. Wang, Y. Xu, and W. Xie, Achieving better accuracy with less computations: A delay-doppler spectrum matching assisted active sensing framework for otfs based isac systems, *IEEE Transactions on Wireless Communications*, vol. 23, no. 6, pp. 6204–6220, 2024.

[17] D. Chen, Y. Zhan, Y. Chen, K. Luo, W. Peng, and W. Wang, Optimal symbol-length filter design for sidelobe suppression in filter bank based orthogonal time frequency space (fb-otfs) systems, *IEEE Transactions on Signal Processing*, vol. 73, pp. 3094–3106, 2025.

[18] M. F. Keskin, C. Marcus, O. Eriksson, A. Alvarado, J. Widmer, and H. Wymeersch, Integrated sensing and communications with mimo-otfs: Isi/ici exploitation and delay-doppler multiplexing, *IEEE Transactions on Wireless Communications*, vol. 23, no. 8, pp. 10 229–10 246, 2024.

[19] N. Wu, H. Li, D. He, A. Nallanathan, and T. Q. S. Quek, Integrated sensing and communication receiver design for otfs-based mimo system: A unified variational inference framework, *IEEE Journal on Selected Areas in Communications*, vol. 43, no. 4, pp. 1339–1353, 2025.

[20] T. Zou, F. Wang, W. Xu, Y. Zhang, M. Pan, and Z. Han, Joint precoding and reflection optimization for irs-assisted mu-mimo-otfs downlink systems, *IEEE Transactions on Vehicular Technology*, pp. 1–16, 2025.

[21] S. G. Neelam, Low complexity mrc detection of irs-aided single user mimo-otfs, *IEEE Signal Processing Letters*, vol. 32, pp. 1396–1400, 2025.

[22] M. Zhou, F. Chen, M. Xia, C. Liu, F. Ji, and H. Yu, Ziv-zakai bound for mixture distribution parameters estimation in otfs-isac system, *IEEE Transactions on Vehicular Technology*, pp. 1–13, 2025.

[23] K. Ryu, H. Lee, K. Choi, and C.-S. Kim, Frame partitioning and interleaving-based low papr otfs, *IEEE Wireless Communications Letters*, pp. 1–1, 2025.

[24] K. Zhang, W. Yuan, P. Fan, and X. Wang, Dual-functional waveform design with local sidelobe suppression via otfs signaling, *IEEE Transactions on Vehicular Technology*, vol. 73, no. 9, pp. 14 044–14 049, 2024.

[25] G. Song, J. Bai, X. Wang, G. Wei, W. Yuan, and T. Q. S. Quek, Low sidelobe level and papr otfs waveform design for

isac systems, *IEEE Transactions on Communications*, pp. 1–1, 2025.

[26] W. Wu, B. Tang, and X. Wang, Constant-modulus waveform design for dual-function radar-communication systems in the presence of clutter, *IEEE Transactions on Aerospace and Electronic Systems*, vol. 59, no. 4, pp. 4005–4017, 2023.

[27] P. Raviteja, Y. Hong, E. Viterbo, and E. Biglieri, Practical pulse-shaping waveforms for reduced-cyclic-prefix otfs, *IEEE Transactions on Vehicular Technology*, vol. 68, no. 1, pp. 957–961, 2019.

[28] Y. Shi and Y. Huang, Integrated sensing and communication-assisted user state refinement for otfs systems, *IEEE Transactions on Wireless Communications*, vol. 23, no. 2, pp. 922–936, 2024.

[29] A. Correas-Serrano, N. Petrov, M. A. Gonzalez-Huici, and A. Yarovoy, Constant modulus otfs based on zak transform of complementary sequences for joint radar and communications, *IEEE Transactions on Radar Systems*, vol. 3, pp. 1131–1144, 2025.

[30] M. Kollengode Ramachandran and A. Chockalingam, Mimo-otfs in high-doppler fading channels: Signal detection and channel estimation, in *2018 IEEE Global Communications Conference (GLOBECOM)*, 2018, pp. 206–212.

[31] T. Bacchielli, L. Pucci, E. Paolini, and A. Giorgetti, A low-complexity detector for otfs-based sensing, *IEEE Transactions on Wireless Communications*, vol. 24, no. 6, pp. 5227–5240, 2025.

[32] H.-T. Sheng and W.-R. Wu, Time-frequency domain channel estimation for otfs systems, *IEEE Transactions on Wireless Communications*, vol. 23, no. 2, pp. 937–948, 2024.

[33] Z. Gong, F. Jiang, C. Li, and X. Shen, Simultaneous localization and communications with massive mimo-otfs, *IEEE Journal on Selected Areas in Communications*, vol. 41, no. 12, pp. 3908–3924, 2023.

[34] D. Zhao, Z. Dong, D. Cai, J. Wang, Z. Khan, and W. Boulila, Constant envelope otfs waveform design and performance analysis for mobile isac systems, *IEEE Transactions on Vehicular Technology*, pp. 1–10, 2025.

[35] A. Kumar, S. Majhi, and H. Li, Sensing and channel estimation for otfs-isac system with reduced papr, *IEEE Communications Letters*, pp. 1–1, 2025.

[36] K. Zhong, J. Hu, H. Li, Y. Wang, X. Cheng, X. Cheng, C. Pan, K. C. Teh, and G. Cui, Joint design of power allocation and unimodular waveform for polarimetric radar, *IEEE Transactions on Geoscience and Remote Sensing*, vol. 63, pp. 1–12, 2025.

[37] K. Zhou, D. Li, S. Quan, T. Liu, Y. Su, and F. He, Sar waveform and mismatched filter design for countering interrupted-sampling repeater jamming, *IEEE Transactions on Geoscience and Remote Sensing*, vol. 60, pp. 1–14, 2022.

[38] K. Zhou, S. Quan, D. Li, T. Liu, F. He, and Y. Su, Waveform and filter joint design method for pulse compression sidelobe reduction, *IEEE Transactions on Geoscience and Remote Sensing*, vol. 60, pp. 1–15, 2022.

[39] K. Zhong, J. Hu, Z. Zhao, X. Yu, G. Cui, B. Liao, and H. Hu, Mimo radar unimodular waveform design with learned complex circle manifold network, *IEEE Transactions on Aerospace and Electronic Systems*, vol. 60, no. 2, pp. 1798–1807, 2024.

[40] F. Wang, S. Feng, J. Yin, C. Pang, Y. Li, and X. Wang, Unimodular sequence and receiving filter design for local ambiguity function shaping, *IEEE Transactions on Geoscience and Remote Sensing*, vol. 60, pp. 1–12, 2022.

[41] P. Gong, J. Liu, X. Cheng, Y. Wu, W. Liu, and J. Liang, Frequency-invariant beampattern synthesis for wideband mimo radar under nulling and papr control, *IEEE Transactions on Vehicular Technology*, vol. 73, no. 6, pp. 7949–7961, 2024.

[42] K. Zhong, H. Jia, R. Wang, J. Hu, K. C. Teh, J. Liu, Y. Wang, H. Li, C. Li, and X. Yu, Design of discrete-phase orthogonal waveforms for cognitive mimo systems, *IEEE Transactions on Cognitive Communications and Networking*, pp. 1–1, 2025.

Author biography

Jiawei Feng received the B.S. degree in communication engineering from the University of Electronic Science and Technology of China, Chengdu, China, in 2022, where he is currently pursuing the M.S. degree in communication engineering. His research interests focused on signal processing and waveform design for radar and communication systems.

Jinfeng Hu received the Ph.D. degree in signal and information processing from the University of Electronic Science and Technology of China, Chengdu, China, in 2005, where he is currently a Professor of Signal and Information Processing with School of Information and Communication Engineering. His research interests include multipleinput multiple-output radar signal processing, phased array radar, adaptive signal processing, machine learning, and artificial intelligence.

Kai Zhong received his B.S. degree and Ph.D. degree in Information and Communication Engineering from the University of Electronic Science and Technology of China (UESTC), Chengdu, China, in 2019 and 2024, respectively. From 2023 to 2024, he was a joint Ph.D. student with the School of Electrical and Electronic Engineering, Nanyang Technological University, Singapore. He is currently a postdoctoral researcher in Information and Communication Engineering at UESTC. His research interests include resource allocation and waveform design for radar and communication systems.

Xiangqing Xiao received the B.S. degree from the University of Electronic Science and Technology of China (UESTC), Chengdu, China, in 2020, where he is currently pursuing the Ph.D. degree with School of Information and Communication Engineering, UESTC. His research interests include waveform design for radar system, signal processing, and deep learning.

Jiacheng Gou received the B.S. degree in electronic information engineering from the University of Electronic Science and Technology of China (UESTC), Chengdu, China, in 2021. He is currently working toward the Ph.D. degree with the School of Information and Communication Engineering, UESTC, Chengdu, China. His research interests include signal processing, machine learning, and parametric array.

Kaizhi Ruan was born in Hunan, China, in 1985. He is currently a senior engineer at Shanghai Electro-mechanical Engineering Institute, Shanghai 201109, China. His research interests include the design and simulation of air defense missile weapon systems.

Yiran Zhang was born in China in 1990. He received the master's degree from the University of Electronic Science and Technology of China in 2017. He is currently a Senior Engineer with the National Key Laboratory of Aircraft Agile Design / Chengdu Aircraft Design Institute. His research interests include radio frequency simulation, waveform design, and digital twin technologies.

Jun Liu was born in China in 1975. He received the bachelor's degree in testing technology and instruments from the Department of Testing Technology and Instruments, Xidian University, Xi'an, China. He currently works with the 41st Institute of China Electronics Technology Group Corporation, Qingdao, China, as a Researcher, mainly engaged in electronic testing technology research and product development.